The International Journal of Advanced Manufacturing Technology (2024) 135:3129–3146
https://doi.org/10.1007/s00170-024-14697-z

ORIGINAL ARTICLE

Influence of a suboptimal environment and sintering temperature on the mechanical properties of fused filament fabricated copper

Scott Downard[1] · Ethan Clark[1] · Cheosung O'Brien[1] · Bita Soltan Mohammadlou[2] · Antonios Kontsos[3] · Dino Celli[4] · Lucas Smith[4,5] · Essa Al Amiri[1] · Andrew Weems[1] · Brian Wisner[1]

Received: 30 August 2024 / Accepted: 16 October 2024 / Published online: 25 October 2024

Abstract

Metal injection molding (MIM) processes are generally more cost-effective for the generation of metallic AM components. However, the thermal processing required to remove the polymer and sinter the metal powder is not well understood in terms of resulting mechanical response and damage evolution, especially in ambient atmospheres where contamination is present. This study aims to provide a range of achievable mechanical properties of copper produced using a MIM-based method called fused filament fabrication (FFF) that is post-processed in a nonideal environment. These results showed direct correlations between sintering temperature to multiple aspects of material behavior. In addition, Nondestructive Evaluation (NDE) methods are leveraged to understand the variation in damage evolution that results from the processing, and it is shown that the higher sintering temperatures provided more desirable tensile properties for strength-based applications. Moreover, these results demonstrate a potential to tailor mechanical properties of FFF manufactured copper for a specific application.

Keywords Additive Manufacturing · Acoustic Emission · Nondestructive Evaluation · Copper · Fused filament fabrication · Sintering

Glossary

Additive Manufacturing

Fused filament fabrication	3D printing process in which material is pre-processed into filament spools and extruded through a heated nozzle onto a flat build plate in a series of layers (analogous to metal injection molding)
Direct Drive	Filament is fed through the nozzle from a location on the printing head itself
Direct Energy Deposition	3D printing process where a material is fed onto a surface while a high energy application method, typically a laser, is supplied to melt material as it is being supplied
Selective Laser Melting	Also known as laser powder bed fusion, 3D printing process in which a layer of powder is repeatedly spread over a flat surface and specific patterns of the powder are melted with a laser
Binder Jet	3D printing method where a layer of powder is applied to a flat surface and a binding ink is extruded over the powder in layered patterns

✉ Brian Wisner
bwisner@ohio.edu

[1] Mechanical Behavior of Materials Group, Center for Advanced Materials Processing, Russ College of Engineering and Technology, Ohio University, Athens, OH 45701, USA

[2] College of Engineering, Drexel University, Philadelphia, PA 19104, USA

[3] Digital Engineering Hub, Henry M. Rowan College of Engineering, Rowan University, Glassboro, NJ 08028, USA

[4] Airforce Research Laboratory, Wright Patterson Airforce Base, Dayton, OH 45433, USA

[5] ARCTOS Technology Solutions, Beaver Creek, OH 45431, USA

Non-Destructive Evaluation	
Acoustic Emission	Applying sensors to a material surface to detect vibrations caused by unknown sources within the material
Digital Image Correlation	Technique of recording a material's surface to track the movement of individual regions of the surface simultaneously

1 Introduction

Additive Manufacturing (AM) processes provide unique benefits over traditional manufacturing processes. AM methods have the potential to generate near-net shapes of complex geometry with little to no tooling across material systems [1, 2]. For metals, there are a range of different methods such as selective laser melting (SLM), direct energy deposition (DED), and metal injection molding (MIM) techniques like binder-jet and fused filament fabrication (FFF) that have been developed to achieve metallic components with a focus on different features. For example, Laser Powder Bed Fusion (LPBF), a form of SLM, can provide good spatial resolution [3], while binder jet methods are more cost-effective but have lower spatial resolution [4]. Moreover, while advances in the use of a range of materials across print modalities including the ability to modify chemical composition during printing [5, 6] have made AM attractive for various applications, limitations still exist in the use of the methodologies for critical components.

By nature, AM processes produce parts layer by layer, and in the case of the most common metallic processes such as LPBF and DED, the printed part is made with a process equivalent to repetitive micro-welds, producing components with more complex thermal histories compared with the ones observed in more traditional subtractive manufacturing methods which can also cause substantial microstructural changes. Other AM processes including many of the MIM-based processes such as FFF and binder jet avoid the complex thermal history issue by using a method to bind the metal powder together in conjunction with chemical and thermal post-processing to remove the binder after printing which also provides the energy to sinter the metal powder together. This allows for a lower cost process with a more uniformly supplied thermal history, typically at the cost of spatial resolution.

Many different metals have proven feasible to be produced by AM techniques. For example, 316 stainless steel and Ti-6Al-4 V have been manufactured using SLM [7–9], DED [10], binder-jet [11, 12], and FFF [2, 9, 13–18]. FFF specifically, has also been used to produce nickel-based alloys [19, 20], tool steel [21], bronze [22], and multiple materials blends [19, 23]. Similarly, copper has been previously evaluated for AM purposes and has been produced by SLM [24], FFF [2, 25–30], micro-extrusion [31], and even cold spraying [32]. Since the FFF produced components typically exhibit higher porosity than those produced by SLM or DED, printing studies have been conducted to reduce the effects caused by the print process to porosity in FFF copper [33] and assess its viability for complex aerospace components [34]. Though for FFF metal processes, the printing is not the only source for altering the resulting properties of the material.

A highly variable aspect in previous work involves the post-processing procedures used for FFF metal components. These processes are unique in terms of furnace environment, furnace temperatures, and whether additional processes such as a chemical debinding step were implemented. For the previously mentioned metal extrusion studies involving copper, sintering studies [25, 26, 29, 31] were performed in an inert gas atmosphere with many also utilizing a chemical debinding process [25, 26, 29]. However, processing in ambient environments has been also reported [27, 28, 32], which was found to introduce contaminants to the produced AM parts. However, none of the previous studies involving ambient sintering of AM copper specifically targeted material variation in their study due to the thermal post-processing itself.

Nondestructive methods including Acoustic Emission (AE) and Digital Image Correlation (DIC) are used to evaluate the mechanical behavior and damage evolution. Both methods have been demonstrated to be useful in understanding material behavior in a range of material systems produced in multiple manufacturing methods [35–38]. Multiple studies evaluated AM materials using AE for the purposes of damage detection and progression during mechanical loading [8, 10, 39], though limited work has been done to leverage AE monitoring to evaluate the effect of AM process variations on resulting material behavior. This work evaluates the effects of peak sintering temperature on material behavior when the process is performed in ambient conditions that are known to result in contaminants. The presence of such contaminants and defects including porosity that result from ambient environment sintering on the material and mechanical properties of the resulting copper samples by leveraging a combination of microscopy and mechanical testing methods coupled with nondestructive evaluation techniques. Given the applications for FFF manufacturing techniques are generally lower-cost and regularly targeted towards private consumers or low-quantity industry production, it is imperative to understand the resulting material achievable in this method with a complementary low-cost processing method, as well as the limitations of such a material. To this end, a comprehensive study of the effect of the sintering temperature in a nonideal, i.e., ambient, environment on material defects and resulting properties is presented here.

2 Material and methods

2.1 Sample printing

The FFF technique was utilized to manufacture all samples later used for density/shrinkage, hardness, and tensile testing-related measurements. All samples were printed using a Creality Ender 3 Pro with a Creality Original Ender 3 Direct Drive Upgrade Kit, which utilized the same printing head and feeding stepper motor as is standard on the original series Ender printers but mounts the motor directly above the printing head. This helped to reduce the length of filament between the feeding gear stepper motor and extrusion nozzle, which reduced filament buckling and breaking and prevented the need for the recommended filawarmer, which is used to combat the brittle nature of the filament. The filament used was produced by Virtual Foundry and consists of greater than 87 wt% copper powder with the remaining weight consisting of polylactic acid (PLA) and trace amounts of 2-Propenenitrile, polymer with 1,3-butadiene and ethenylbenzene. Additionally, a proprietary binding agent was used which claimed to improve print quality. As recommended by Virtual Foundry, a 0.6 mm hardened steel nozzle was used as opposed to the Creality Ender 3 Pro's default 0.4 mm brass nozzle.

The printing parameters seen in Table 1 were used for all types of samples. Printing settings were modified through a series of preliminary tests to find the values reported in Table 1. The printing layout for each layer of these samples consisted of three wall layers followed by an alternating 45° angle line infill pattern per layer set to 100%, an example print layout can be seen for a dog bone tensile specimen in Fig. 1. It should be noted that with the utilized flow rate, the material was being fed faster than necessary to print samples. This resulted in extra material needing to be removed from the samples during printing. The overfed was necessary

Table 1 Utilized print settings compared to Virtual Foundry recommendations

Parameter	Virtual Foundry recommendations	Study settings
Filawarmer	Yes	No
Print speed (mm/s)	60	20
Nozzle size (mm)	0.6	0.6
Nozzle material	Hardened Steel	Hardened Steel
Nozzle temp (°C)	205 – 235	235
Bed temp (°C)	40 – 50	55
Flow rate (%)	N/A	145%
Layer height (mm)	N/A	0.2
Layer width (mm)	N/A	0.4
Infill overlap (%)	N/A	30

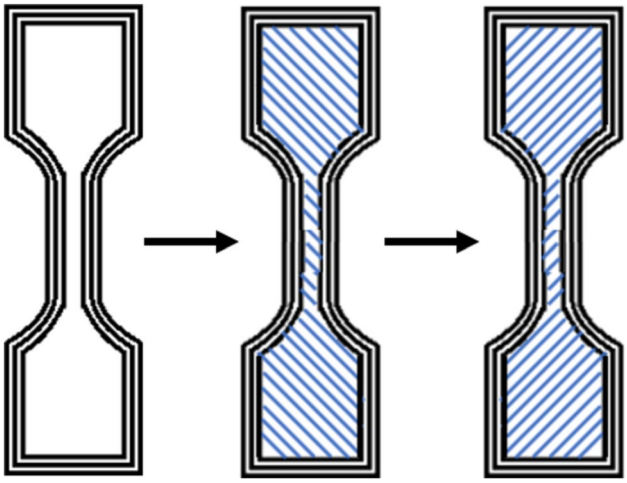

Fig. 1 Tensile sample printing layup

to prevent additional porosity from the printing process as discussed by [33]. In addition to the high flow rate, the slicing software was also given the assumption that the nozzle was still 0.4 mm, meaning that the 0.6 mm nozzle would be slightly overhanging onto previous print lines which helped to remove the large triangular-shaped pores shown at the wall-infill boundary in the previous printing study [33].

All samples were sliced using the UltiMaker Cura software. The quantities of samples produced were as follows: 24 shrinkage discs, 12 hardness discs, and 32 tensile dog bones. Shrinkage discs were modeled with a diameter of 10 mm and the same thickness as the dog bone samples to inform on the expected density of the dog bone samples but with a geometry that is more accurately measurable. Hardness discs were printed with a diameter of 20 mm and thickness of 3.5 mm. The dog bone samples were based on ASTM D638 Type V [40] specimens with dimensions shown in Fig. 2; however, the samples were printed with a uniform volume increase of 105% to allow for shrinkage during the sintering process. Samples with visually identifiable surface defects, or ones with defects that were observed during printing, were not used for this study.

2.2 Furnace post-processing

Heat treatments for samples include a two-step thermal debind and sinter process. The same furnace, a Lindberg/Blue 51,894 box furnace equipped with a SYL 2352P PID controller, was used for all thermal processes. All samples were processed in an ambient atmosphere ranging from 17 to 25 °C and 50 to 90% humidity depending on the day. Alumina crucibles measuring 110 mm tall, 26 mm inner diameter, and wall thickness of 4 mm, with an equal thickness lid, were used for shrinkage disc and dog bone samples. Hardness discs used a different size crucible of the same

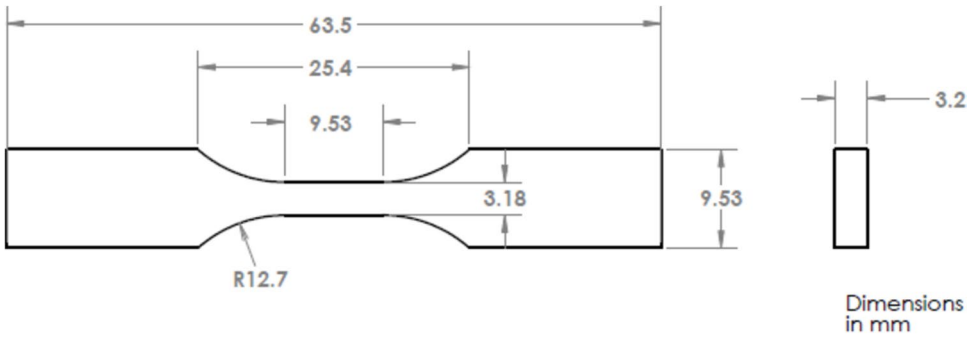

Fig. 2 ASTM D638 Type V Sample Geometry [40]

material, with a height of 125 mm, 112 mm inner diameter, and wall thickness of 4 mm with a lid of the same thickness to allow for sintering of more samples at a time under the same thermal conditions. The debinding process used aluminum oxide (Al_2O_3) powder as the packing ballast and the sintering process used magnesium silicate (talcum) powder along with sintering carbon, all of which were procured and recommended by Virtual Foundry. For debinding, Al_2O_3 filled the crucible and received no additional compression. For sintering, talcum powder was compacted by hand with a 2.38 kg weight with a base diameter of 76 mm; no additional downward force was applied by hand. Talcum powder filled all the crucibles except for the top 5 mm which was occupied by uncompacted sintering carbon.

Shrinkage discs were processed with four samples per crucible; two rows of two samples were orientated with their circular faces vertical. Rows were offset 90° from one another and the two samples per row had their circular faces parallel with one another. The two rows were equally spaced between the top of the packing material and bottom of the crucible. This orientation was kept the same for debinding and sintering.

Hardness discs were processed with three samples per crucible. All three samples were placed in a single horizontal plane at the midpoint of the crucibles height and arranged in a triangular pattern with their circular faces horizontal and parallel to one another. This orientation was kept the same for debinding and sintering.

Dog bone samples were processed with two samples per crucible. These samples were placed vertically in a row with their wide faces parallel and both of their centerlines even with the centerline of the crucible. This orientation was kept the same for debinding and sintering.

The thermal process programs used for both debinding and sintering are shown in Fig. 3; debinding was kept the same for all samples. For sintering, the peak temperature was changed as the independent variable of this study. Shown in Fig. 3 is the control sintering process whose peak

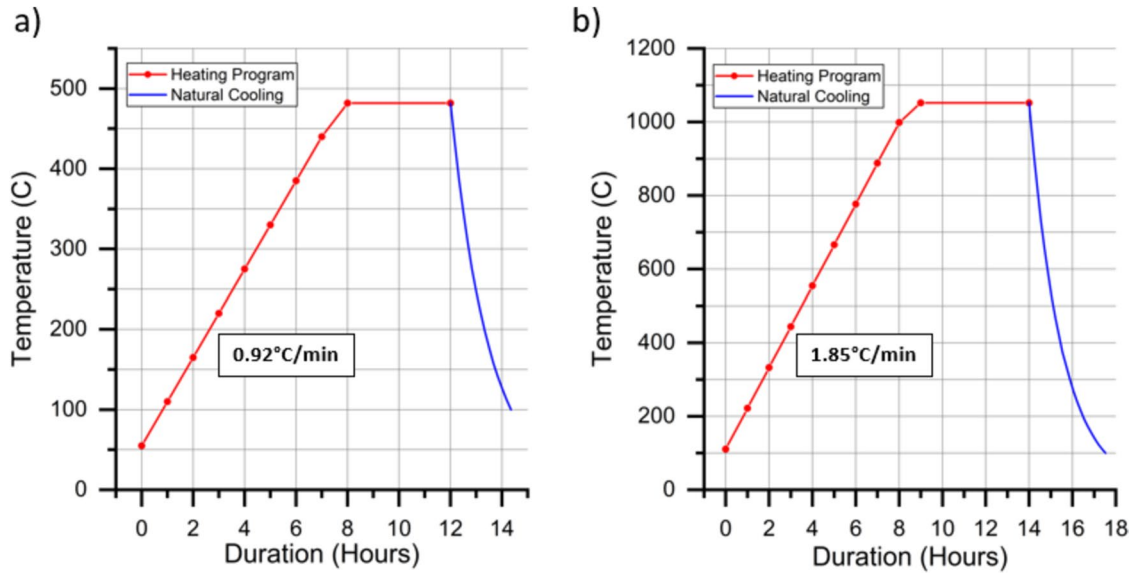

Fig. 3 **a** Debinding thermal process. **b** Control sinter thermal process

temperature of 1052 °C and was the recommendation of Virtual Foundry. The other conditions of this study are referred to as low and high, which peak sintering temperatures of 1024 °C and 1080 °C, respectively. The heat ramp duration prior to the peak temperature hold was kept the same between conditions, resulting in a slight variation in ramp rate. This final heating segment ramp rate to the peak sintering temperature was 0.42, 0.88, and 1.35 °C/min for the sinter conditions low, control, and high, respectively. The cooling rate of the furnace was found based on temperature measurements taken after furnace shutdown following a control sintering process and let to naturally cool to ambient air temperature over an 8-h period. These points were then used to create an exponential fit curve based on Newton's law of cooling and had an R^2 value fit to the collected data of 0.993.

2.3 Tensile testing

Tensile testing was conducted on seven samples of each sintering condition and three of the original seven green samples due to them incurring damage before testing. The green samples are used for a baseline. Engineering stress and strain were used from the tests to determine the values of yield stress (S_y), ultimate stress (S_{ult}), Young's modulus (E), and elongation at failure (ϵ_{fail}). Both S_y and E were calculated based on 0.2% offset criteria as specified in [41]. The S_{ult} was the peak stress measured from each test, and the ϵ_{fail} was determined as the point of strain when the stress had reduced by 10% of S_{ult} after S_{ult} had occurred, again based on [41]. The universal testing system (UTS) will be started with in situ DIC and AE. The DIC strain over time will be measured using a virtual extensometer over the sample's gage section and synced to the UTS data using polynomial curve fits.

Dog bone samples were mechanically tested using an Instron 5567 equipped with a 30kN load cell. The samples were loaded in displacement control at 0.5 mm/min based on [41]. Force was balanced prior to loading samples and displacement was zeroed prior to initiating crosshead displacement for each test. The crosshead displacement will not be used for strain in the results, opting to utilize the virtual extensometer values collected in post-processing on the gage section of samples using DIC.

2.3.1 DIC setup

A speckle pattern was produced using a base layer of white spray paint with black dots supplied by an airbrush over the entire gage length for DIC. Prior to testing, each sample was pretensioned to a peak of 60% of S_y to help prevent slipping of the sample under tension which was followed by recording an initial set of 5 DIC images to provide strain error. Images during the test were obtained at 0.5 fps using the Aramis 2.3Mpx stereo system equipped with Titanar 75 mm lenses from GOM. A subset and step size of 0.78 mm and 0.4 mm was used for all samples producing a peak strain noise of 0.0397% across all samples based on the arithmetic mean of the reference frame's surface components.

2.3.2 AE setup

AE was monitored using a Pico wideband sensor (150–750 kHz) with a 30 dB threshold. The sensor was attached using hot glue in the location shown in Fig. 4, both the location and sensor were kept consistent through testing. A Pencil Led Break Test (PLBT) was performed to validate sensor functionality and correct coupling. All signals were amplified uniformly across all frequencies using a 2/4/6 Preamplifier set to 40 dB gain and recorded on a PCI-8 Express Data acquisition board running AEWin software at 10 million samples per second (MSPS) to avoid signal aliasing. All signals were analog filtered on acquisition between 100 kHz and 1 MHz which represents the closest built-in filter to the sensor range. Waveforms were captured using a Peak Definition Time (PDT), Hit Definition Time (HDT), and Hit Lockout Time (HLT) of 50, 300, and 300 µs, respectively. All post-processing was completed using Noesis 12.0 software for feature extraction after applying a 10th order Digital Butterworth Bandpass filter to the ideal recording frequencies of the sensor (150–750 kHz) with a 6 dB adaptive threshold. It should be noted that in addition to the filtering applied

Fig. 4 Green dog bone with attached pico sensor

to the data, there was an additional threshold added during post-processing due to hits with a predominantly low signal to noise ratio. Because of this, all data with a post-filtered amplitude below 26 dB were removed.

2.4 Shrinkage discs procedure

All 24 shrinkage discs were measured for thickness and outer diameter in the as-printed (green) state as well as each of their respective sintering states. Dimensions were measured using calipers which could measure to the nearest 0.01 mm and masses were recorded using an OHAUS Discovery DV241C balance. Densities were calculated based on the discs cylindrical volume and mass. Eight discs were sintered from the original 24 green discs to each of the three sinter states to ensure repeatability and a normal distribution is achieved.

2.5 Hardness discs procedure

There were 12 hardness discs prepared for testing, three for each condition. Each disc was tested after polishing up to 1200 grit with a silicon carbide wheel. Vickers hardness (HV) was used to evaluate the hardness of each disc using a load of 50 g-force. Rockwell Hardness testing was attempted using a Page-Wilson Corporation model B523T Rockwell hardness tester set to the E scale; however, data could not be obtained on any Rockwell scale we expect due to the collapsing porosity of the samples. Microhardness testing was conducted on a LM300AT in multiple regions of each disc as shown in Fig. 5. Each zone spanned 1/3rd of the disc's radius and measurements were taken in random patterns throughout the zones to obtain a general hardness value.

2.6 Fractography imaging

A VHX7000 series digital microscope was used at a magnification of 80× on all fracture surfaces. The images were segmented using the provided analysis software based on brightness to find the pores that are present. The segmented images were then used to quantify the porosity present on the fracture surface as an area ratio.

2.7 MicroCT scanning parameters

Micro-computed tomography (MicroCT) scans were conducted using a Carl Zeiss Xradia 620 Versa system to acquire the data. The scanning parameters were precisely configured, with a voltage set at 140 kV and power at 21W, resulting in a spatial resolution of 9.04 µm achieved through a 0.4X detector. During data collection, 2402 projection numbers were acquired, and an HE2 filter was implemented to enhance imaging quality by minimizing noise. Following data acquisition, raw projection data were reconstructed using Zeiss's XRM reconstructor software. This involved employing standard center shift and beam hardening correction techniques to ensure accuracy. The resultant images were refined through Gaussian filtration to optimize segmentation quality. Segmentation was performed using ORS Dragonfly Pro software, which utilized a thresholding method supplemented by manual correction for precision. Quantitative analysis was then carried out to evaluate pore characteristics such as size,

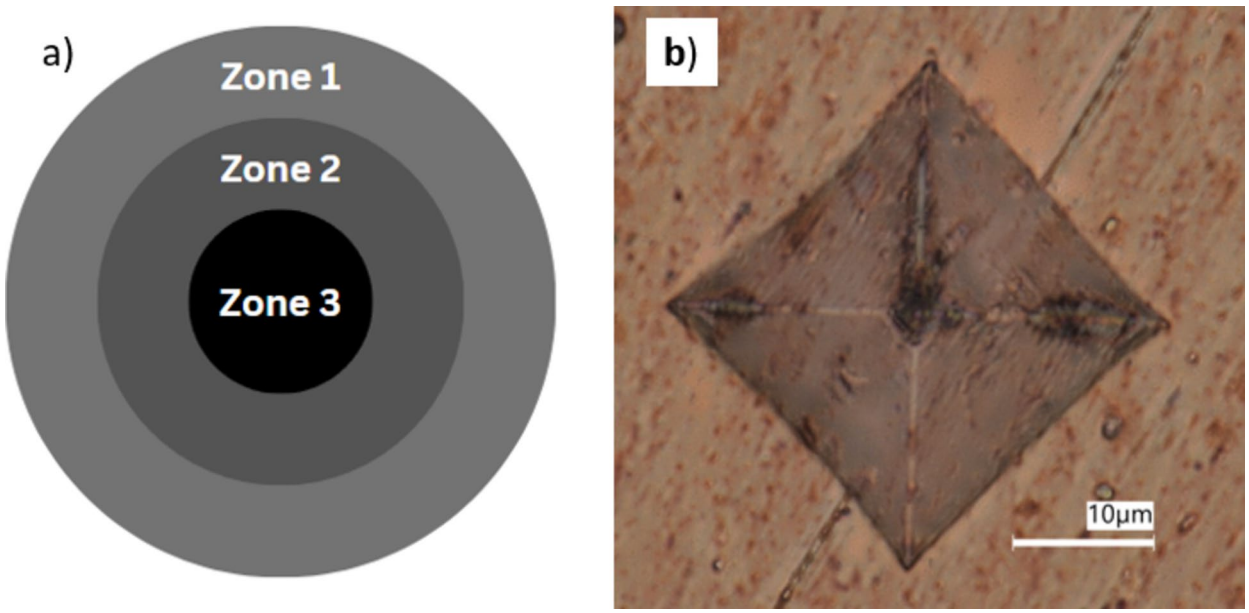

Fig. 5 **a** Microhardness disc indentationzones. **b** Microhardness indentation at 50 g-force on high sinter sample

shape, and distribution within the material. These results were then contrasted with density and fracture images to identify differences in mechanical properties.

2.8 Chemical composition

After sintering, samples were imaged on a Thermo Fisher Scientific Phenom XL G2 desktop scanning electron microscope system equipped with energy dispersive spectroscopy (EDS). Element identification software performed EDS to analyze regions of interest on each sample. High-resolution mapping scans were completed at the center and on the edge of the samples at approximately 300 × magnification to quantify the elements present after debinding and sintering. Results of these scans provided weight concentration data for each element that was found in the specific region of the sample that was imaged, providing key insight into the effectiveness of each sintering process and allowing comparison to the ideal alloy.

2.9 Statistical comparisons

For each resulting dataset, statistical comparisons will be made between the three sintered conditions to verify the presence of any significant differences resulting from the thermal process variation. Two-tailed One-Way ANOVAs were conducted using Minitab Statistical Software using $\alpha = 0.05$.

3 Results and discussion

3.1 Density changes and porosity

The initial filament used for this study contains a maximum of 13 wt% polymer and binder materials that are thermally degraded and removed, resulting in a reduction in sample size. Table 2 and Fig. 6 show the results of the manufactured discs used for this analysis that were measured immediately following both printing and sintering steps to avoid potential differences as a result of atmosphere changes which can be particularly problematic in the green condition. Figure 6 also compares the green and sintered density results to pure annealed copper [42]. The green samples show a low density as compared to all sinter conditions as expected by the presence of the additives and the larger volume than present in the sintered states. This low variation in density indicates that the printing process is stable and repeatable across all samples. The high sinter samples were found to have the highest density and lowest variation across all sinter conditions while the control samples produced the lowest shrinkage and highest variation. This improved consistency is expected as the higher temperature would provide additional energy to assist with diffusion of the copper particles and results in a stronger connection.

Table 2 Mean shrinkage disc results for each tested condition

Condition	N samples	Volume (cm^3)	Volumetric shrinkage (%)	Density (g/cm^3)
Low	8	0.219 ± 0.007	31.2 ± 1.4	6.31 ± 0.22
Control	8	0.217 ± 0.005	29.5 ± 1.6	6.41 ± 0.15
High	8	0.211 ± 0.002	31.1 ± 0.5	6.57 ± 0.11
Green	24	0.306 ± 0.003		5.03 ± 0.06

In comparison to the green samples, all sinter conditions show an increase in density as the PLA and binders are removed and mostly copper remains. Comparison of the density between sinter conditions shows that the high sinter condition exhibits the highest density with the smallest variation as expected based on volume loss. Following the same logic, it would be expected for the control condition to have the lowest density since it exhibited the least shrinkage; however, it is the low sinter condition which shows the lowest density and highest variation between the sintered conditions. While the low sinter condition exhibits a lower density and high variation as expected, this is counter to the observed shrinkage where the control sample shrinks in comparison to both high and low sinter conditions. This would indicate that the reason for the lower density is the result of a lack of diffusion between copper particles resulting in a likely increase in porosity in both the control and low sinter conditions. Statistical results showed a significant difference in high sintered density in comparison to both low and control conditions, with p-values of 0.010 and 0.027, respectively. Figure 7 shows an example of the shrinkage observed in the dog bone samples as they are going from green, debound (brown), and finally sintered for the control condition, as well as the sintered dog bone sample in its polished state prior to uniaxial testing. The shrinkage results and this figure show that while the dog bone samples were printed to match ASTM-D638 Type V [40] specimens, the final tensile specimens were approximately 90% the scale of dimensions provided in Fig. 2.

The level of porosity in the gage section from each condition can be seen in Fig. 8, and Table 3 numerically shows the difference in pores between conditions. All detected pores that were less than three pixels were removed from the results. Views in Fig. 8 are from side views that are parallel to the FFF printing layer lines where there is a clear elongation of the pores in line with the printing layers. Figure 8a–c shows all pores identified while Fig. 8d–f shows only the largest 30 voids recorded.

When looking at the present voids in all samples, regardless of condition, it is clear they all contain large quantities of both large and small voids. There is no clear trend in the porosity of the samples in each condition from the single

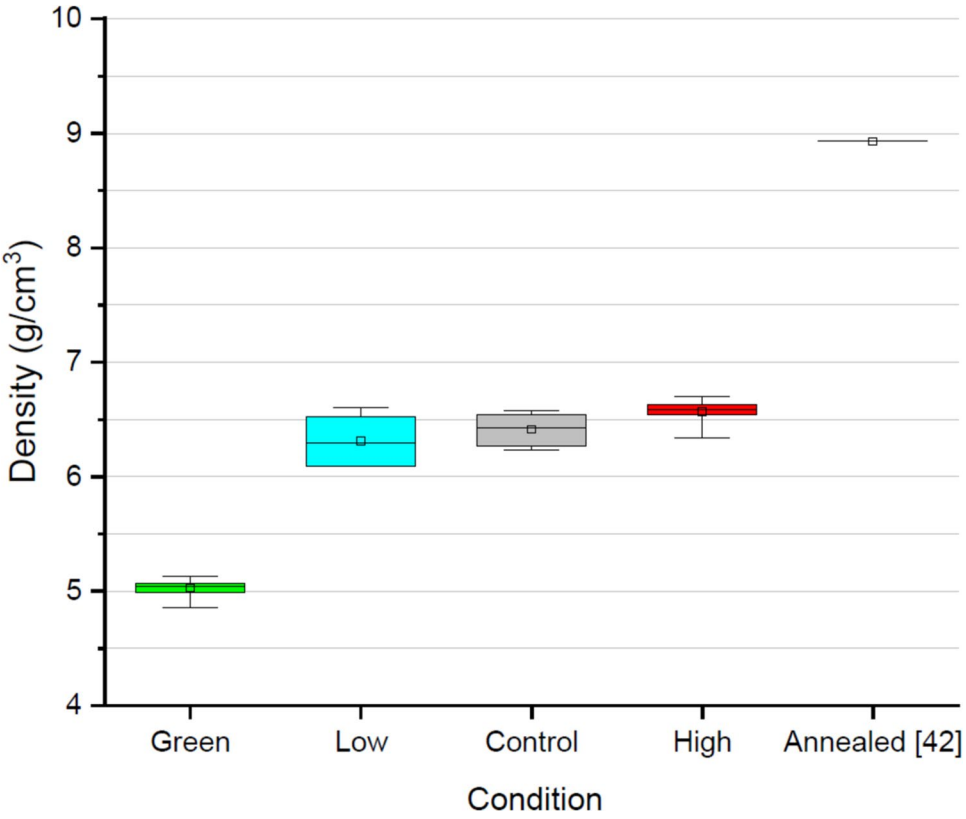

Fig. 6 This study's shrinkage disc density results compared to previous literature value of annealed pure copper [42]

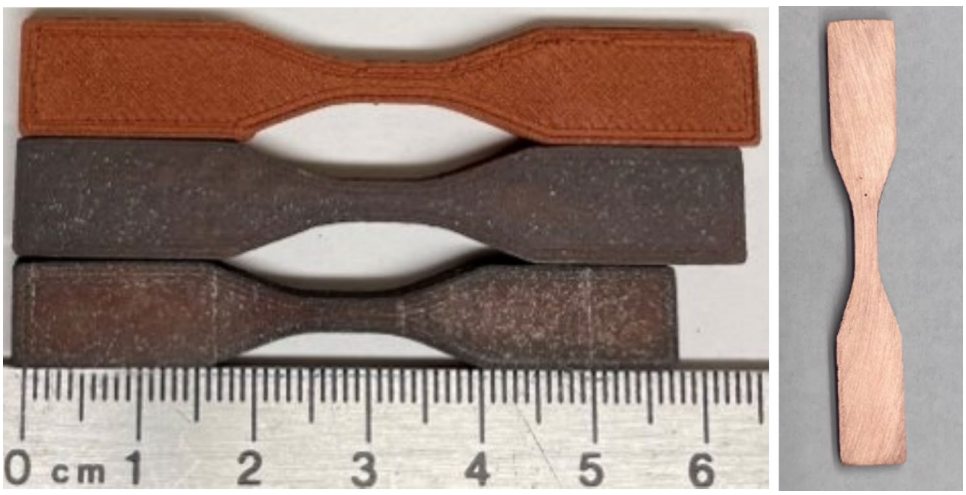

Fig. 7 Dog bone sample shrinkage example, (top) green, (middle) brown, (bottom) control sintered, along with (right) polished dog bone sample(not to scale)

scan, but rather it shows the extensive porosity present as a result of the manufacturing method that cannot be removed from an increase in sintering temperature alone. The use of pressure would likely help reduce the porosity further but was not a part of the scope.

3.2 Hardness

Rockwell hardness results could not be obtained on any Rockwell scale. This can be explained by the low density and high porosity as compared to annealed copper discussed in the previous section. It is expected that during indentation, the pores below the top surface collapsed under the applied loads making it impossible to record a reliable reading. Micro-hardness results were able to be obtained as they interrogate a smaller region of the material, and the results reveal the similarities between the material produced in the sintering process and those obtained on annealed pure copper [42]. The sintered samples show a downward trend in hardness as the sintering temperature increased. Results of

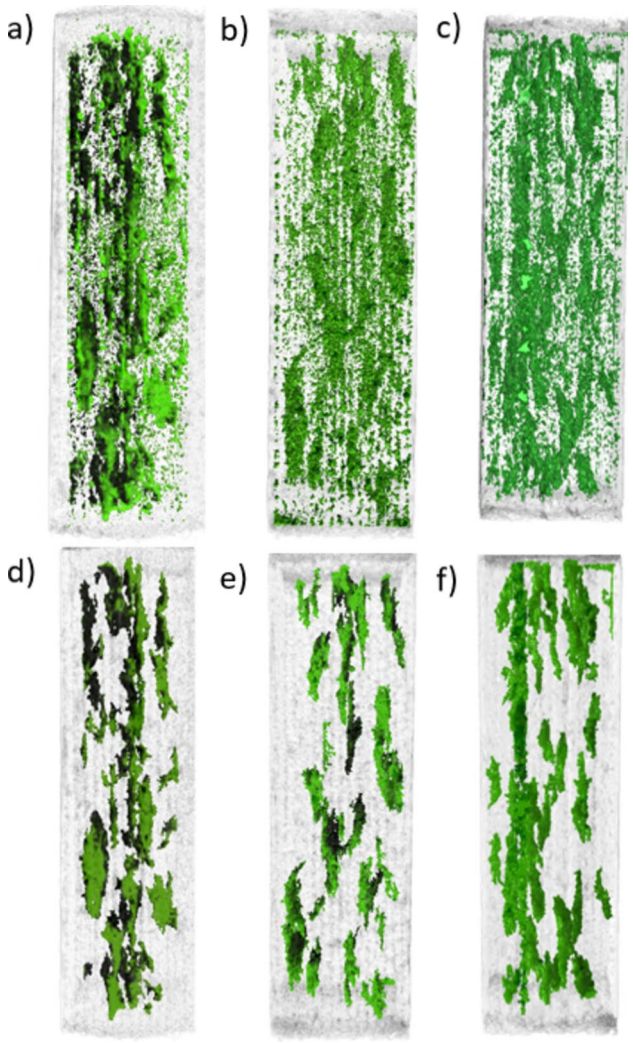

Fig. 8 CT scan dog bone gage section porosity. **a** Low sinter all pores. **b** Control sinter all pores. **c**High sinter all pores. **d** Low sinter top 30 volume pores. **e** Control sinter top 30 volume pores. **f** High sinter top 30 volume pores

the HV hardness testing can be seen in Table 4. When the overall results of sintered conditions were compared, low sinter was significantly different than control and high sintered conditions, with both resulting *p*-values equal to 0.000. Figure 9 compares the results of green and all sinter condition samples hardness to annealed pure copper [42].

Table 3 CT scan porosity results of copper dog bone gage sections

Sintered sample	Pore count	Overall porosity (%)	Total pore volume (mm^3)	Top 30 pore volume (mm^3)
Low	9844	3.07	1.919	1.585
Control	10,225	2.31	1.738	1.300
High	12,107	3.09	2.322	1.784

As all heating and hold times remained the same and only the hold temperature changed, the reduction in hardness is likely a result of the furnace cooling process that would be slower for a sample that is cooling from a higher temperature. This would allow for more annealing to occur as the furnace cools naturally resulting in slightly longer times between 200 and 400 °C. The results indicate that this process of obtaining additively manufactured copper can result in hardness values on par with traditionally manufactured copper.

3.3 Tensile behavior

The higher density coupled with a lower hardness indicates that the high sinter condition should be more ductile and have higher yield and ultimate strengths compared to the other two conditions. The monotonic tensile behavior revealed such generally expected differences between the behavior of different sinter conditions. The stress–strain plots in Fig. 10 show each sample of the three sintered dog bone conditions. From the tensile testing, S_y, S_{ult}, E, and ε_{fail} were extracted to be compared to both green samples and literature values of traditional annealed copper [42] in Table 5 showing a clear mechanical advantage for the high sinter condition in comparison to the other sinter conditions. Given the variability in E for these materials, mean values of E and S_y are provided with the variability as inner quartile range (IQR) as opposed to S_{ult} and ε_{fail} which are provided with standard deviation.

No significant differences were seen in S_y or E between any sintering conditions; however, high sintered samples were significantly different than both low and control sintered samples in terms of S_{ult} and ε_{fail}. No *p*-value of these four comparisons exceeded 0.004; there was nearly a significant difference in S_{ult} values of low and control sinter conditions with a *p*-value of 0.051. All conditions exhibit substantial drops in stress during testing in the plastic deformation region. These drops occur just after the yield point in all conditions, while they also appear near the final fracture in the low sinter condition. Additionally, this behavior is less prevalent in the high sinter condition and does not occur in annealed copper as demonstrated by [43]. While these drops are not expected in traditionally manufactured copper material, they can be explained when compared to other material systems that are additively manufactured or in lattice-type structures [44, 45]. These load drops are consistent with materials that experience incremental failures or serrations in their stress–strain curves as the area carrying the load fails and the stress gets redistributed in the material [46–48]. In this case, the porous structure resulted in many voids that grow and coalesce such as seen in [48, 49]. When these coalesced pores reach a critical size, a large fracture event of the primary load pathway can occur resulting in a sudden release of energy that is observed as a

Table 4 HV hardness results for sintered and green discs

Condition	N samples	Measurements per zone	Zone 1	HV Zone 2	50 Zone 3	Overall
Low	3	30	65.5 ± 15.6	72.7 ± 22.8	69.1 ± 28.4	69.1 ± 23.1
Control	3	30	54.5 ± 16.0	55.6 ± 10.5	55.1 ± 12.0	55.1 ± 13.0
High	3	30	50.9 ± 13.4	51.4 ± 11.6	55.1 ± 15.6	52.4 ± 13.8
Green	3	9	102.6 ± 26.3	111.4 ± 29.6	102.2 ± 33.3	105.4 ± 30.1

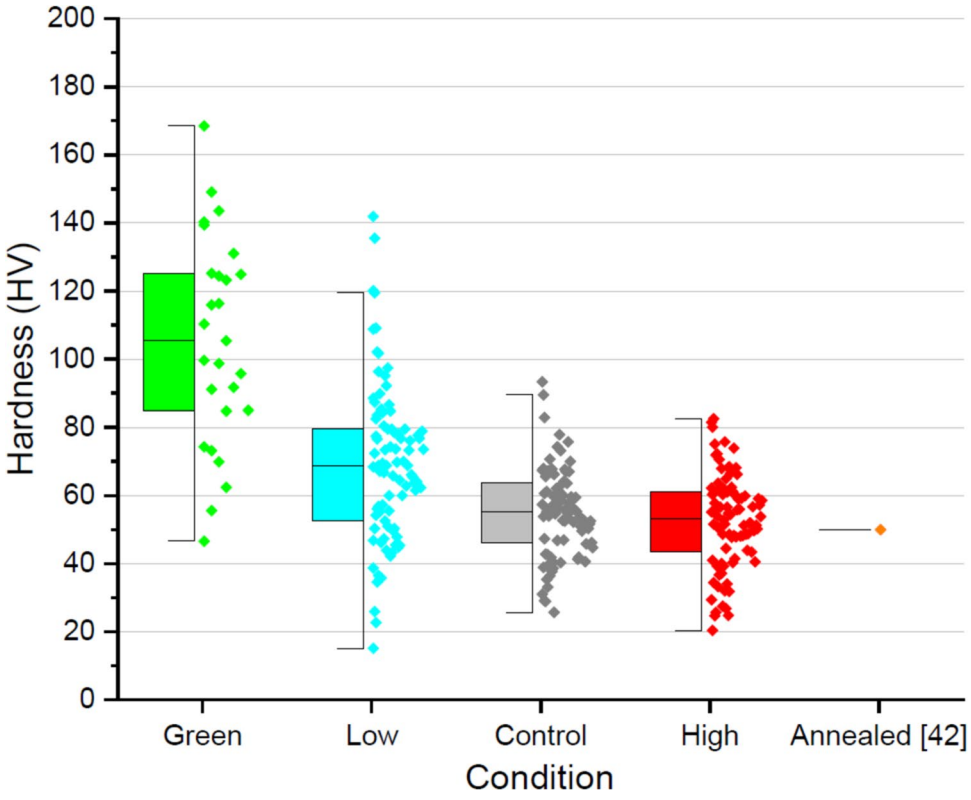

Fig. 9 This study's microhardness by condition in comparison to previous literature value of annealed pure copper [42]

sudden drop in the load-carrying capacity of the material in a displacement-controlled test. Once the stresses are redistributed to new load paths in the remaining material the load will increase as before [48]. The high sinter condition shows less of this effect because of the higher density that results in more load paths existing at the start of the test making any load drops less severe. In addition to the load behavior over the load curve, the difference in the ultimate tensile strength and the stress at failure can be seen in Fig. 11a and b which shows the high sinter condition exhibiting improved strength and ductility as compared to the other conditions. Moreover, each condition exhibited differences in mean strength as quantified in Table 5; however, as a result of variation, there is overlap observed between the behavior of all conditions particularly in the range of 8–9% strain in Fig. 11a and b where all three conditions are present.

Another potential cause of variation within the tensile specimens is the presence of contaminants from our ambient thermal process as mentioned by [22, 23, 27]. To quantify the potential influence of contaminants within our samples, EDS was conducted on the fracture surface of the control sintered dog bone condition. The elemental composition of the dog bone's gage section was measured at the outer edge and core, while this measurement quantity is not enough to provide a full representation of the sample population, it is sufficient to acknowledge the presence of contaminants that contribute to the final wt%. The results near the surface (edge) and in the center (core) of the sample are shown in Table 6 for the three primary elements present. The quantity of oxygen present is from a combination of the ambient air exposure and from the degradation of the PLA binder, which is primarily composed of oxygen and carbon. It is clear that the concentration of the contaminants is higher near the surface than the core and that these will result in material properties that are not the same as pure copper; however, the presence of the contaminants that result from this sintering

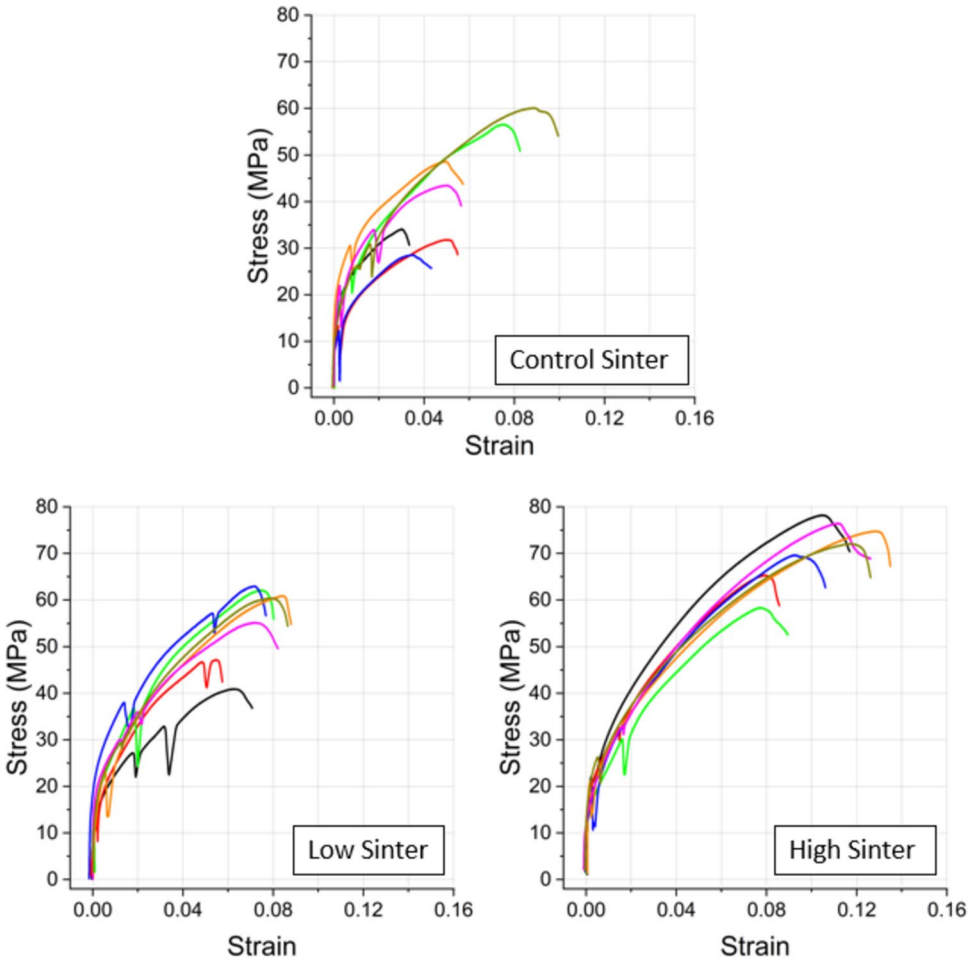

Fig. 10 Stress–strain curves for all tested samples and conditions

Table 5 This study's tensile parameter results based on sample condition compared to literature values of annealed pure copper [42]

Sinter condition	N samples	Sy (MPa)		E (GPa)		Sult (MPa)	ε at fail (%)
		Mean	IQR	Mean	IQR		
Low	7	19.4	2.7	28.9	16.0	55.7 ± 7.9	7.7 ± 1.0
Control	7	18.8	4.4	26.3	15.1	43.3 ± 11.5	6.1 ± 2.1
High	7	21.0	2.5	56.4	42.4	70.7 ± 6.5	11.2 ± 1.8
Green	3	4.4	0.3	11.1	10.6	6.2 ± 0.9	0.4 ± 0.2
Annealed pure copper [42]		33.3	-	110	-	210	60

process in ambient conditions demonstrates mechanical properties that are in the range of pure copper and could allow for the method to be used in similar applications.

3.4 Nondestructive evaluation results

Variation in AE activity was observed not only between conditions on average, but also within each condition. This is expected based on the variability in porosity and subsequently the stress–strain behavior that is common in additively manufactured components [16, 50, 51]. Figure 12 shows the variation in the form of AE absolute energy accumulation across and within sinter conditions where each row is a different sinter condition. The columns represent the test results with the least, median, and maximum AE observed AE activity as defined by the number or recorded hits.

In general, the samples that produced the least amount of activity Fig. 12a, d, and g show intermittent instantaneous jumps in energy throughout the loading. In the case of the low sinter condition, this type of activity was observed regardless of the number of AE events recorded suggesting periodic large fracture events occur as expected from the observed stress drops in the stress–strain curve. The control

sinter samples show that there is a more progressive failure process as the amount of AE activity increases. The increase in activity and lack of energy jumps observed particularly in Fig. 12f combined with the lack of any observed stress drop suggests that this material fails more gradually like traditionally manufactured metals typically do and does not have large fracture events resulting from the porosity present. This is further observed in the high sinter conditions where in the median activity case we are seeing a more progressive failure than observed in the other conditions for the same level of defined activity. The difference between conditions can be seen more clearly in Fig. 13 where AE amplitude, peak frequency, and absolute energy for the median AE activity cases.

Figure 13 shows similar frequency bands and a clear reduction in the AE activity in the median case between sinter conditions; however, general trends remain the same in amplitude and peak frequency. As sinter temperature increases, the density also increases allowing for an increase in load pathways and properties that trend to annealed copper [42]. As annealed copper is a highly ductile metal that exhibits minimal AE amplitude as compared to brittle materials as demonstrated by [52, 53], it is expected that as ductility increases AE activity will reduce due to the detectability limit of the method. In this work, an increase in ductility is observed to correlate with the sintering temperature. In all conditions, most of the activity occurs near the yield point of the samples as is consistent with AE observed in metal fracture [38, 54, 55]. This trend is strongest in the high sinter condition that shows activity reduces drastically just after yield which is consistent with AE observations in metallic materials [38, 56] where crack nucleation activity is concentrated at this point. As with previous observations, this trend indicates an improved bond between the sintered copper particles with an increase in sinter temperature [57, 58]. While there is a reduction in activity in the high sinter case, the energy continues to grow gradually over the life of the sample suggesting that there is progressive growth occurring after the nucleation at yield. Both the control and

Table 6 EDS elements wt% results of control sinter dogbone fracture surface

Location	Elemental wt%		
Cu	C	O	
Edge	61.44	30.72	7.32
Core	69.82	25.30	4.88

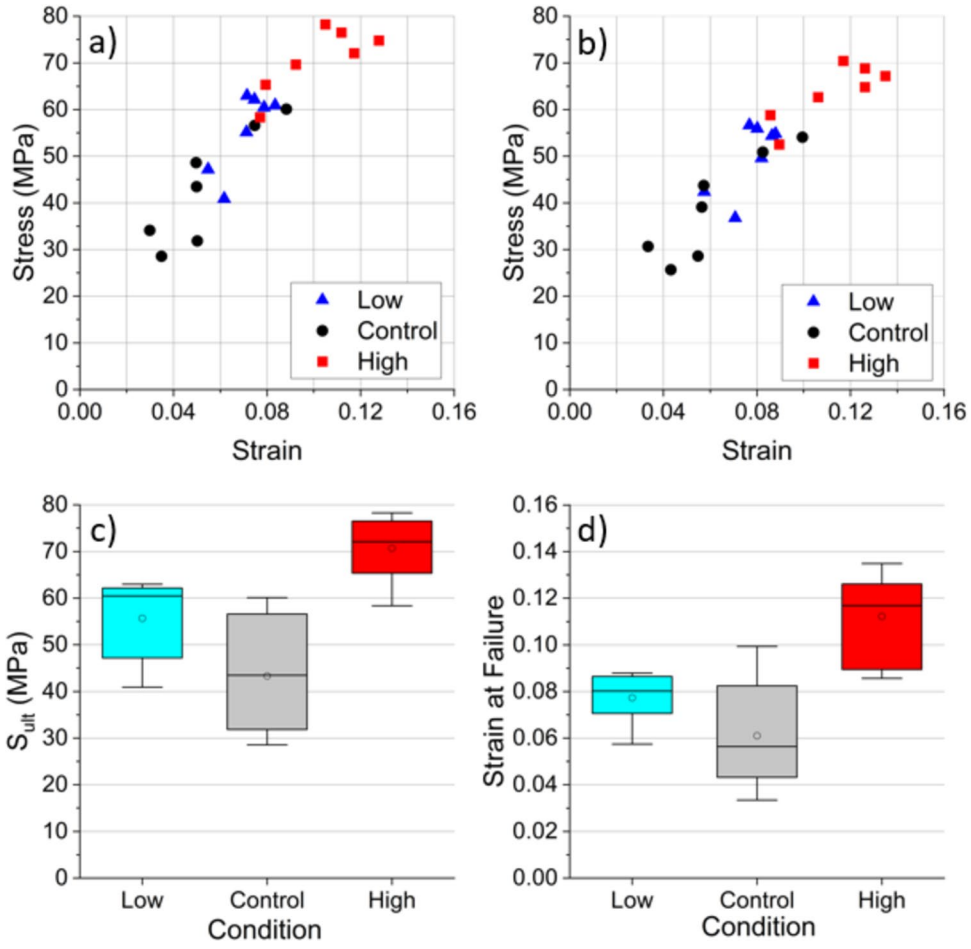

Fig. 11 **a** Location of ultimate stress per sample. **b** Locations of failure per sample. **c** Ultimate stress distributions. **d** Failure strain distributions

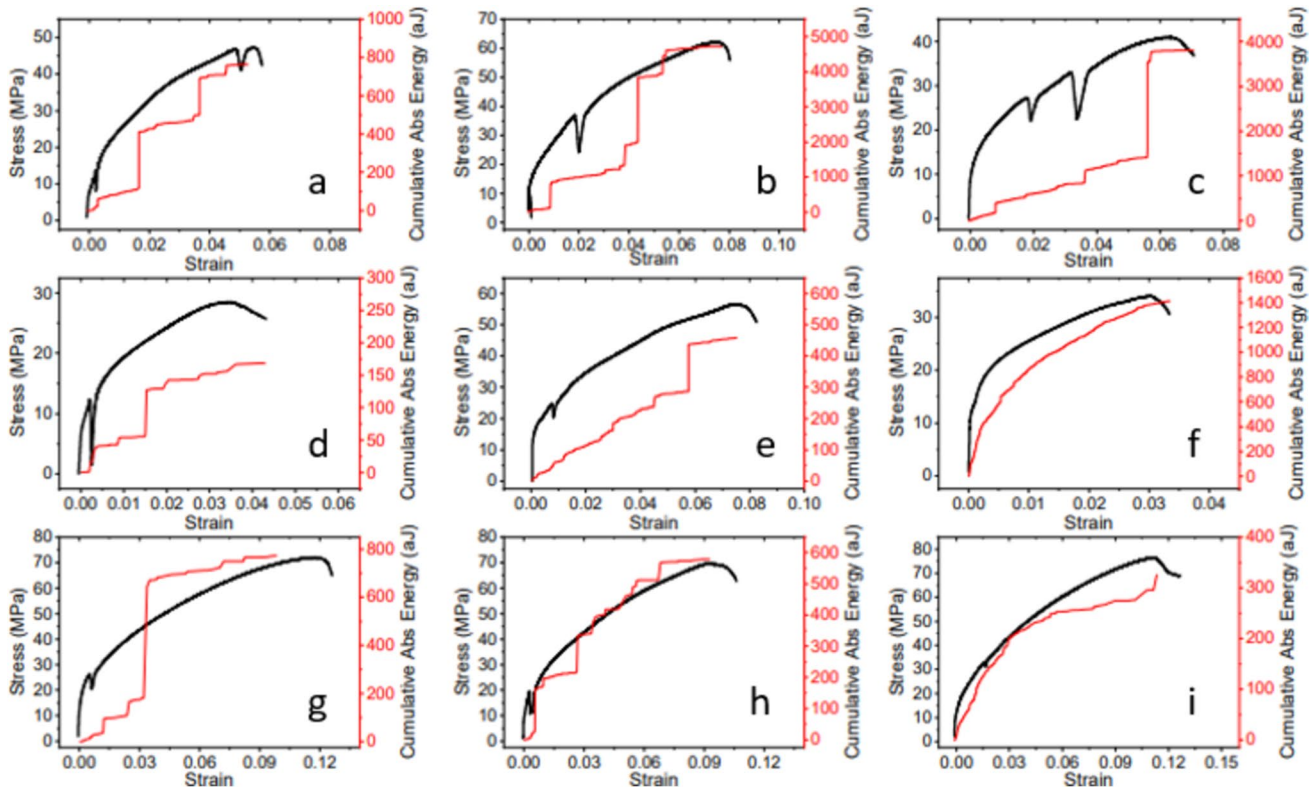

Fig. 12 Minimum, median, and maximum AE hit quantity sample for each condition, filteredcumulative absolute energyoverlayed on stress–strain curves. Rows represent from top to bottom: low sinter, control sinter, high sinter. Columns from left to right: least, median, maximum hits

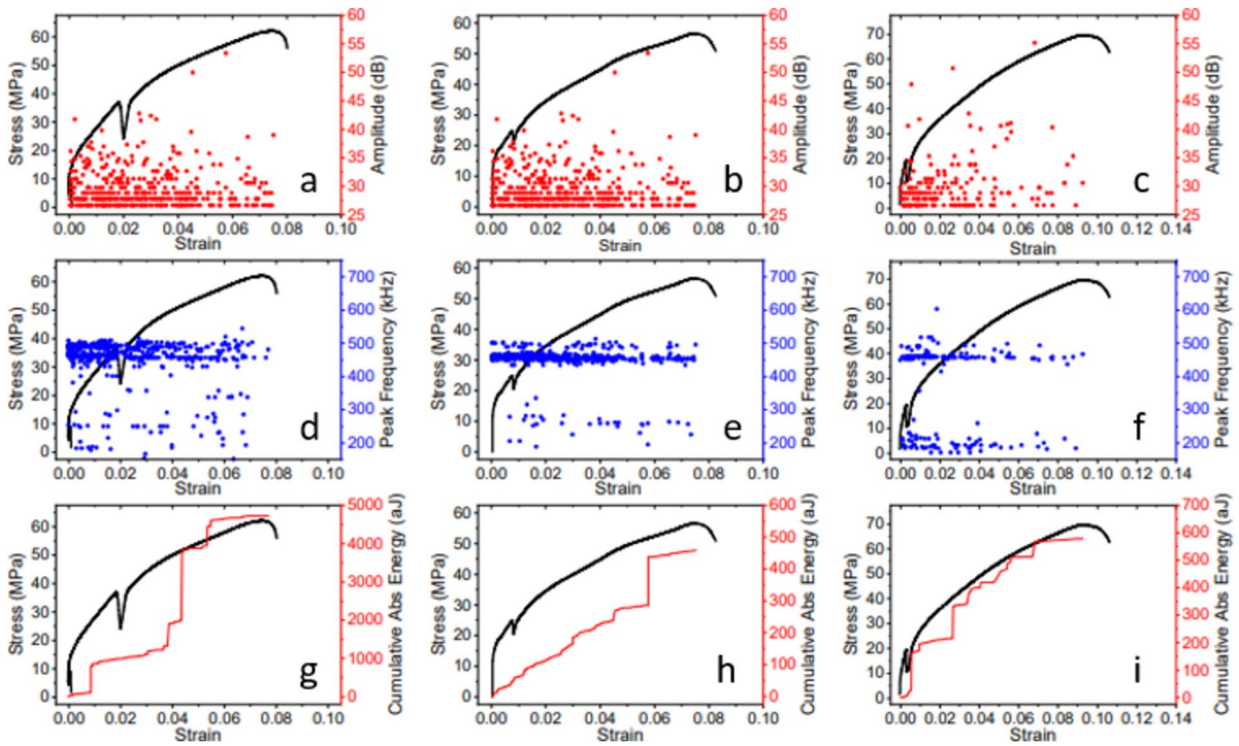

Fig. 13 Amplitude, peak frequency, and cumulative absolute energy comparisons between median hitquantity samples of each sintercondition. **a**, **d**, **g** Low sinter median. **b**, **e**, **h** Control sinter median. **c**, **f**, **i** High sinter median

Table 7 AE energy results

Condition	N samples	Mean Abs Energy (aJ)	Median Abs Energy (aJ)	Mean cumulative Abs Energy (aJ)
Control	7	1.82	0.37	914.63
Low	7	29.79	0.33	17,417.18
High	7	2.77	0.52	443.71

Table 8 AE condition variation

Condition	Min hits	Max hits	Median hits	Mean hits
Control	100	2250	433	847.7
Low	258	1490	527	663.9
High	88	445	184	247.0

low sinter conditions show relatively consistent activity in the amplitude and peak frequency up to the ultimate strength before dying off indicating crack nucleation and brittle type failures occur to a much later stress than observed in the high sinter condition. The most notable AE trends were seen in the energy outputs of the samples, which are quantified in Table 7 and are based on the mean across all samples in each condition. The most notable differences in this data include the total energy and absolute energy per hit of the low samples being on a different order of magnitude in comparison to other conditions. However, the median energy per hit has the lowest value on the low sinter, which suggests that this condition resulted in a lot of low energy hits with a few high energy hits likely from significant brittle-like failure resulting from a weaker particle bond during sinter that dominates the total energy trend. With the results shown in Table 8, it should also be noted that the results of each sample, within the same condition, were highly variable. Table 8 shows the range of hit quantities that were seen across samples of the same condition. For both Tables 7 and 8, the data shown is representative of the full tensile test and not only on hits prior to the ε_{fail} cut-off. It may appear that there were clear differences between the cumulative absolute energy between sintered conditions, statistical results showed no significant differences, this is due to the high variability in the AE activity of the low condition causing significantly large failure events in inconsistent quantities across samples. In terms of hit quantities, only the high and low sinter conditions show statistically significant differences with a p-value of 0.038.

3.5 Fractography

Each sample's fracture surface was observed using optical microscopy with the only difference in surfaces being the

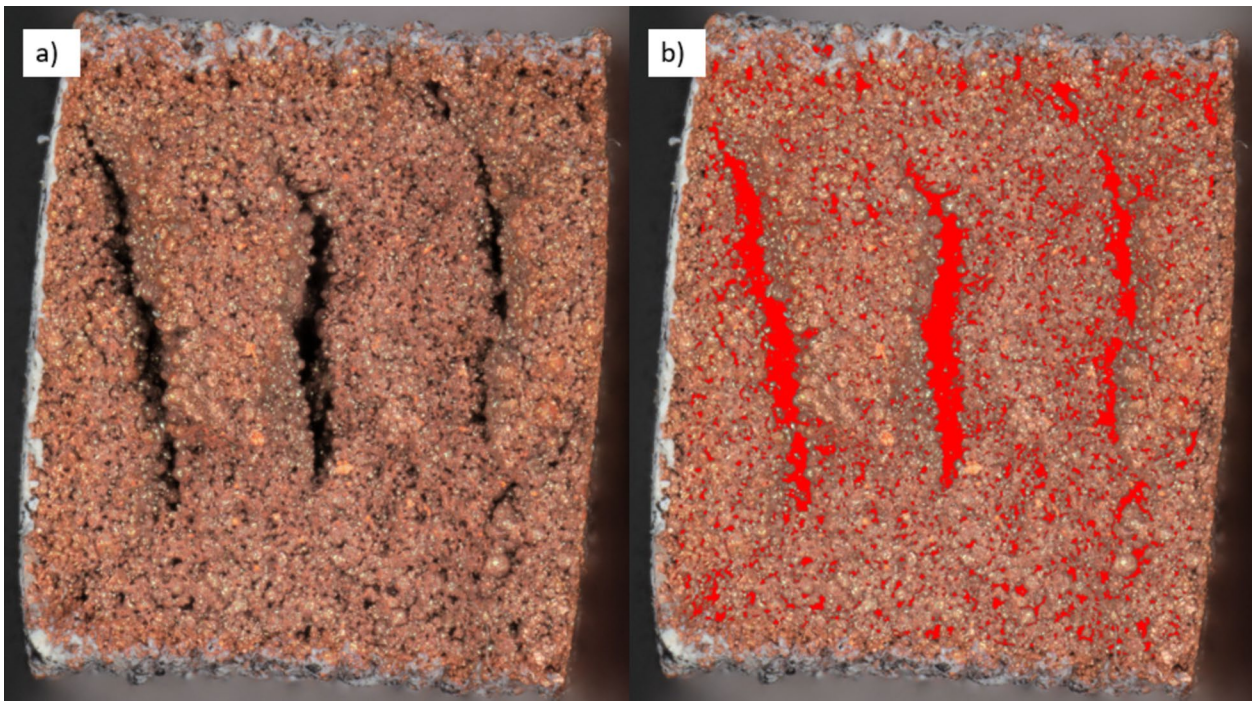

Fig. 14 Porosity map example. **a** Keyence fracture surface image and **b** same image with regions considered pores highlighted in red

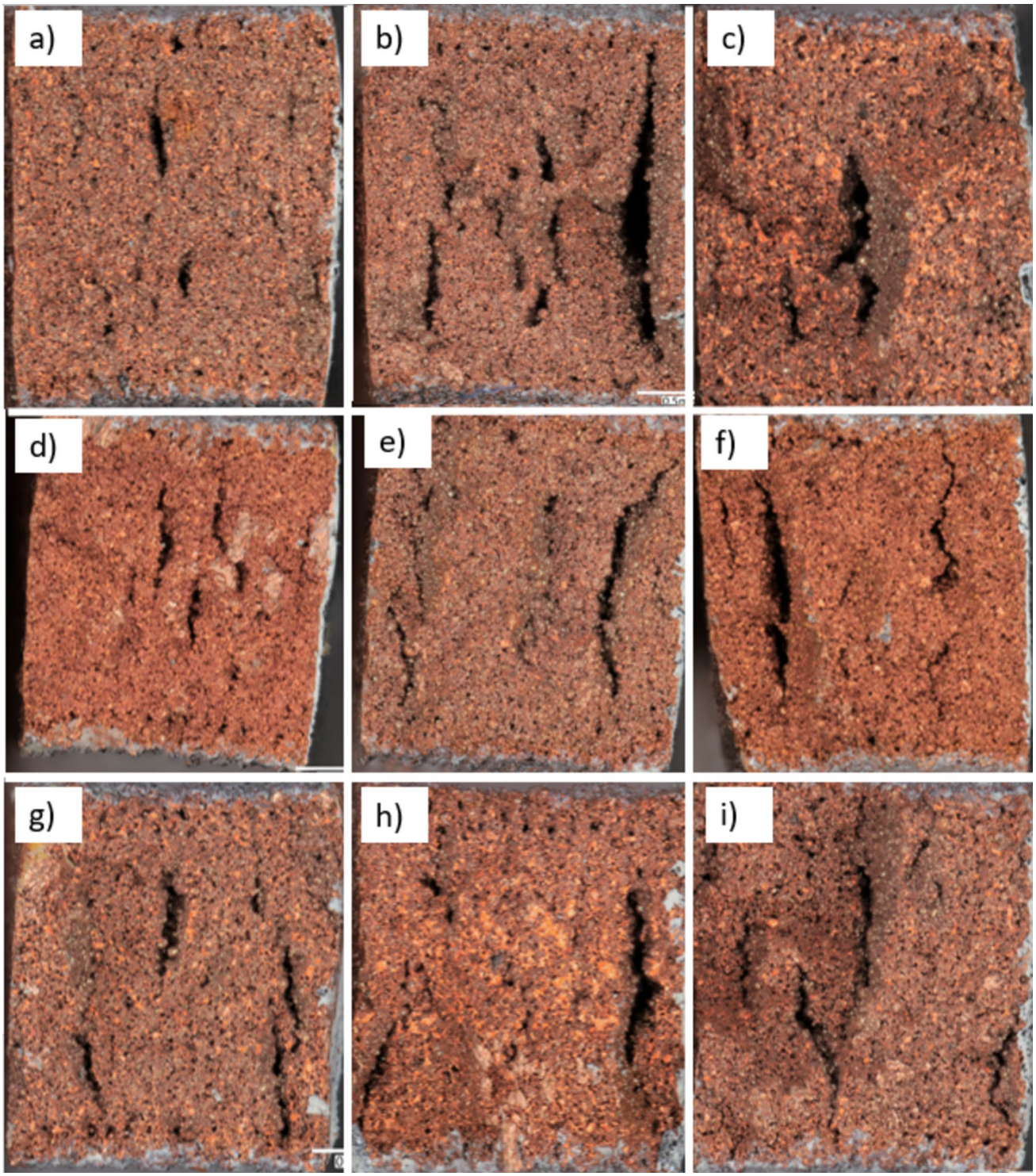

Fig. 15 Bottom fracture surfaces of dog bone samples based on porosity. Rows represent from top to bottom: low sinter, control sinter, high sinter. Columns from left to right: least, median, maximum porosity

distribution of voids. No difference in fracture initiation sites was observable. The voids on both fracture surfaces of each sample were extracted using an overlayed polygonal map after tensile testing for further analysis. A void is defined here as any area inside the materials bounding box that has no material. Figure 14 shows an example of the porosity map where the regions highlighted in red in Fig. 14b are the areas considered to be pores. These are the final voids after

Table 9 Fracture surface porosity results show mean values of condition using averaged top and bottom porosities to represent each sample

Condition	N samples	Porosity (%)	Quantity pores	Pore size (μm^2)	Total map area (μm^2)	Total pore area (μm^2)
Low	7	15.572 ± 3.407	14,231	73.574	6.7E + 06	1.0E + 06
Control	7	13.372 ± 2.045	11,494	78.543	6.7E + 06	8.9E + 05
High	7	12.825 ± 1.479	9293	90.365	6.4E + 06	8.3E + 05

mechanical loading and thus can be used to compare the presence of the combination of initial and evolved voids in the material. They cannot, however, be directly correlated to initial porosity.

Figure 15 shows the difference in bottom fracture surfaces across all three sinter conditions. Values from the top and bottom surfaces were averaged together to create an overall value for each sample; the mean values of each condition were calculated and results of which can be seen in Table 9. No statistically significant difference was seen between the fracture surface porosity of the samples.

When comparing the fracture surface porosity measurements with the total AE absolute energy and hits during testing, no correlation can be observed. Supporting the hypothesis that AE activity is primarily based upon the strength of bonds created between copper particles due to changes in sintering temperature and not due to internal pore growth with the exception of the large load drops that result from such failure.

The porosity results follow the same trend as hardness where the higher sintering temperature sees the lowest porosity as well as the fewest number of pores per sample, which also agrees with the higher density and improved mechanical properties over the other conditions. The fracture surfaces and values show that the control condition generally has less pores compared to the low condition, but a larger pore size that can explain the control condition's generally lower mechanical properties than observed in the low condition. These trends presented in Table 9 are also not consistent with the results of the CT scan of the dog bone cross sections. From the CT scans, the control sinter sample had a higher pore quantity but lower total pore volume than the low condition. The high sinter condition is also on the opposite end of the porosity and pore count extremes in CT scans in comparison to fracture porosity. The discrepancies of the porosity before and after loading can be used to examine the evolution of said pores as a result of the loading where the pores grow more in the control and high sinter conditions than they do in the low condition over the course of the loading which would explain the progressive failure observed in AE. Moreover, this could be an indication of the superior bonds between individual copper particles and subsequent higher quality sintering achieved by the high sinter temperature but would need more CT samples to ensure the trends there are consistent. Based on the density values alone, it was expected that the mechanical properties of the control would be better than the low; however, it is shown here that the presence of porosity is not sufficient to explain the behavior. While initial pore position and geometry greatly contribute to the material response, the evolution of these pores as a response to the loading appears to have the final say in the resulting material behavior.

4 Conclusion

This study has provided a deeper understanding and clearer expectations of achievable mechanical properties utilizing this low-cost manufacturing technique. And while this material cannot be used in the same range of applications as copper produced by traditional or other AM methods, it does show a future for more accessible AM methods for metals. Results demonstrate the mechanical response and material properties obtained from sintering FFF copper in a two-step process without a controlled environment yield vastly different properties compared to traditionally manufactured copper as well as other AM methods which utilize inert atmospheres. Within our study, slight variations in sintering temperatures reveal signification variation in mechanical behavior when processed in otherwise identical conditions. Direct correlations existed between sintering temperature to both density and porosity, both of which improved with an increase in temperature. A higher sintering temperature also improved the ductility and altered the damage evolution of the materials based on recorded mechanical data and AE activity, respectively. The increase in AE energy suggests larger more brittle damage occurring with a lower sintering temperature as compared to the higher temperatures. AE frequency bands were consistent across all sintering temperatures, suggesting that while the size and number of damage events vary between conditions, similar damage mechanisms are present within all conditions. Additionally, it is shown that the higher sintering temperature provided overall more desirable tensile properties for strength-based applications while the lower temperatures can provide lower density materials in cases where strength is of less concern. These results show that, while still being quite variable, different mechanical properties of FFF manufactured copper can be acquired by altering the sintering parameters used to process green samples, adding a new variable to further enhance property control beyond the printed structure itself.

Declarations

Competing interests The authors declare no competing interests.

References

1. Cuesta E, Gesto A, Alvarez BJ, Martínez-Pellitero S, Zapico P, Giganto S (2019) Dimensional accuracy analysis of direct metal printing machine focusing on roller positioning errors. Procedia Manuf 41:2–9. https://doi.org/10.1016/j.promfg.2019.07.022
2. Alyammahi MS, Atatreh S, Susantyoko RA, Alkindi T (2021) Evaluation of dimensional accuracy of additively manufactured metal parts in fused filament fabrication process. Volume 6: Design, Systems, and Complexity, American Society of Mechanical Engineers, Virtual, Online. p V006T06A014
3. Nagarajan B, Hu Z, Song X, Zhai W, Wei J (2019) Development of micro selective laser melting: the state of the art and future perspectives. Engineering 5(4):702–720
4. Gokuldoss PK, Kolla S, Eckert J (2017) Additive manufacturing processes: selective laser melting, electron beam melting and binder jetting—selection guidelines. Materials 10(6):672. https://doi.org/10.3390/ma10060672
5. Lefky CS, Gallmeyer TG, Moorthy S, Stebner A, Hildreth OJ (2019) Microstructure and corrosion properties of sensitized laser powder bed fusion printed Inconel 718 to dissolve support structures in a self-terminating manner. Addit Manuf 27:526–532
6. Torbati-Sarraf H, Torbati-Sarraf SA, Chawla N, Poursaee A (2020) A comparative study of corrosion behavior of an additively manufactured Al-6061 RAM2 with extruded Al-6061 T6. Corros Sci 174:108838
7. Chen Y, Gou B, Xu X, Ding X, Sun J, Salje EKH (2023) Multi-branches of acoustic emission as identifier for deformation mechanisms in additively manufactured 316L stainless steel. Addit Manuf 78:103819
8. Strantza M, Aggelis D, De Baere D, Guillaume P, Van Hemelrijck D (2015) Evaluation of SHM system produced by additive manufacturing via acoustic emission and other NDT methods. Sensors 15(10):26709–26725
9. Gong H, Snelling D, Kardel K, Carrano A (2019) Comparison of stainless steel 316L parts made by FDM- and SLM-based additive manufacturing processes. JOM 71(3):880–885
10. Strantza M, Van Hemelrijck D, Guillaume P, Aggelis DG (2017) Acoustic emission monitoring of crack propagation in additively manufactured and conventional titanium components. Mech Res Commun 84:8–13
11. Simchi A, Petzoldt F, Hartwig T, Hein SB, Barthel B, Reineke L (2023) Microstructural development during additive manufacturing of biomedical grade Ti-6Al-4V alloy by three-dimensional binder jetting: material aspects and mechanical properties. Int J Adv Manuf Technol 127(3–4):1541–1558
12. Chen W, Chen Z, Chen L, Zhu D, Fu Z (2023) Optimization of printing parameters to achieve high-density 316L stainless steel manufactured by binder jet 3D printing. J of Materi Eng Perform 32(8):3602–3616
13. Léonard F, Tammas-Williams S (2022) Metal FFF sintering shrinkage rate measurements by X-ray computed tomography. Nondestruct Test Eval 37(5):631–644
14. Varela Ortega, de Seijas M, Bardenhagen A, Rohr T, Stoll E, (2023) Indirect induction sintering of metal parts produced through material extrusion additive manufacturing. Materials 16(2):88514. Ortega Varela De Seijas, M., Bardenhagen, A., Rohr, T., and Stoll, E. (2023) Indirect induction sintering of metal parts produced through material extrusion additive manufacturing. Materials 16(2):885
15. Thompson Y, Gonzalez-Gutierrez J, Kukla C, Felfer P (2019) Fused filament fabrication, debinding and sintering as a low cost additive manufacturing method of 316L stainless steel. Addit Manuf 30:100861
16. Ait-Mansour I, Kretzschmar N, Chekurov S, Salmi M, Rech J (2020) Design-dependent shrinkage compensation modeling and mechanical property targeting of metal FFF. Prog Addit Manuf 5(1):51–57
17. Kan X, Yang D, Zhao Z, Sun J (2021) 316L FFF binder development and debinding optimization. Mater Res Express 8(11):116515
18. Ecker JV, Dobrezberger K, Gonzalez-Gutierrez J, Spoerk M, Gierl-Mayer Ch, Danninger H (2019) Additive manufacturing of steel and copper using fused layer modelling: material and process development. Powder Metall Progress 19(2):63–81
19. Ferro P, Fabrizi A, Elsayed H, Savio G (2023) Multi-material additive manufacturing: creating IN718-AISI 316L bimetallic parts by 3D printing, Debinding, and Sintering. Sustainability 15(15):11911
20. Hasib AG, Niauzorau S, Xu W, Niverty S, Kublik N, Williams J, Chawla N, Song K, Azeredo B (2021) Rheology scaling of spherical metal powders dispersed in thermoplastics and its correlation to the extrudability of filaments for 3D printing. Addit Manuf 41:101967
21. Vetter J, Huber F, Wachter S, Körner C, Schmidt M (2022) Development of a material extrusion additive manufacturing process of 1.2083 steel comprising FFF printing, solvent and thermal debinding and sintering. Procedia CIRP 113:341–346
22. Wei X, Behm I, Winkler T, Scharf S, Li X, Bähr R (2022) Experimental study on metal parts under variable 3D printing and sintering orientations using bronze/PLA hybrid filament coupled with fused filament fabrication. Materials 15(15):5333
23. Mousapour M, Salmi M, Klemettinen L, Partanen J (2021) Feasibility study of producing multi-metal parts by fused filament fabrication (FFF) technique. J Manuf Process 67:438–446
24. Yan X, Chang C, Dong D, Gao S, Ma W, Liu M, Liao H, Yin S (2020) Microstructure and mechanical properties of pure copper manufactured by selective laser melting. Mater Sci Eng, A 789:139615
25. Atatreh S, Alyammahi MS, Vasilyan H, Alkindi T, Susantyoko RA (2023) Evaluation of the infill design on the tensile properties of metal parts produced by fused filament fabrication. ResultsEngineering 17:100954
26. Schüßler P, Franke J, Czink S, Antusch S, Mayer D, Laube S, Hanemann T, Schulze V, Dietrich S (2023) Characterization of the metal fused filament fabrication process for manufacturing of pure copper inductors. Materials 16(20):6678
27. Mohammadizadeh M, Lu H, Fidan I, Tantawi K, Gupta A, Hasanov S, Zhang Z, Alifui-Segbaya F, Rennie A (2020) Mechanical and thermal analyses of metal-PLA components fabricated by metal material extrusion. Inventions 5(3):44
28. Terry S, Fidan I, Tantawi K (2021) Preliminary investigation into metal-material extrusion. Prog Addit Manuf 6(1):133–141

29. Cañadilla A, Romero A, Rodríguez GP, Caminero MÁ, Dura ÓJ (2022) Mechanical, electrical, and thermal characterization of pure copper parts manufactured via material extrusion additive manufacturing. Materials 15(13):4644
30. Wu H, Yu Z, Wang Y (2016) A new approach for online monitoring of additive manufacturing based on acoustic emission. International Manufacturing Science and Engineering Conference, vol 49910. American Society of Mechanical Engineers, Blacksburg, p 8. https://doi.org/10.1115/MSEC2016-8551
31. Kolli S, Beretta M, Selema A, Sergeant P, Kestens LAI, Rombouts M, Vleugels J (2023) Process optimization and characterization of dense pure copper parts produced by paste-based 3D microextrusion. Addit Manuf 73:103670
32. Hutasoit N, Rashid RAR, Palanisamy S, Duguid A (2020) Effect of build orientation and post-build heat treatment on the mechanical properties of cold spray additively manufactured copper parts. Int J Adv Manuf Technol 110(9–10):2341–2357
33. Moritzer E, Elsner CL (2022) Investigation and improvement of processing parameters of a copper-filled polymer filament in fused filament fabrication as a basis for the fabrication of low-porosity metal parts. Macromol Symp 404(1):2100390
34. Uffelmann S, Pestotnik S (2023) Investigation of the manufacturability of a copper coil for use in space components by means of the fused filament fabrication process. CEAS Space J 15(5):701–713
35. Sendrowicz A, Myhre AO, Wierdak SW, Vinogradov A (2021) Challenges and accomplishments in mechanical testing instrumented by in situ techniques: infrared thermography, digital image correlation, and acoustic emission. Appl Sci 11(15):6718
36. Wisner B, Mazur K, Kontsos A (2020) The use of nondestructive evaluation methods in fatigue: a review. Fatigue Fract Eng Mat Struct 43(5):859–878
37. Rao J, Leong Sing S, Liu P, Wang J, Sohn H (2023) Non-destructive testing of metal-based additively manufactured parts and processes: a review. Virtual Phys Prototyp 18(1):e2266658
38. Vinogradov A (1998) Acoustic emission in ultra-fine grained copper. Scripta Mater 39(6):797–805
39. Barile C, Casavola C, Pappalettera G, Vimalathithan PK (2020) Acoustic emission descriptors for the mechanical behavior of selective laser melted samples: an innovative approach. Mech Mater 148:103448
40. "ASTM D638 Standard Test Method for Tensile Properties of Plastics" [Online]. Available: https://compass.astm.org/document/?contentCode=ASTM%7CD0638-22%7Cen-US. Accessed 27 Feb 2024
41. "ASTM E8 Standard Test Methods for Tension Testing of Metallic Materials" [Online]. Available: https://compass.astm.org/document/?contentCode=ASTM%7CE0008_E0008M-22%7Cen-US. Accessed 27 Feb 2024
42. "Copper, Cu; Annealed," MatWeb, https://www.matweb.com/search/datasheet.aspx?matguid=9aebe83845c04c1db5126fada6f76f7e&ckck=1. Accessed 29 Aug 2024
43. Carreker RP, Hibbard WR (1953) Tensile deformation of high-purity copper as a function of temperature, strain rate, and grain size. Acta Metall 1(6):654–663
44. Ćwikła G, Grabowik C, Kalinowski K, Paprocka I, Ociepka P (2017) The influence of printing parameters on selected mechanical properties of FDM/FFF 3D-printed parts. IOP Conf Ser: Mater Sci Eng 227:012033
45. Alsalla H, Hao L, Smith C (2016) Fracture toughness and tensile strength of 316L stainless steel cellular lattice structures manufactured using the selective laser melting technique. Mater Sci Eng, A 669:1–6
46. Zhang Y, Liu JP, Chen SY, Xie X, Liaw PK, Dahmen KA, Qiao JW, Wang YL (2017) Serration and noise behaviors in materials. Prog Mater Sci 90:358–460
47. Zhang L, Guo P, Wang G, Liu S (2020) Serrated flow and failure behaviors of a Hadfield steel at various strain rates under extensometer-measured strain control tensile load. J Market Res 9(2):1500–1508
48. Hastie JC, Koelblin J, Kartal ME, Attallah MM, Martinez R (2021) Evolution of internal pores within AlSi10Mg manufactured by laser powder bed fusion under tension: as-built and heat treated conditions. Mater Des 204:109645
49. Babout L, Maire E, Buffière JY, Fougères R (2001) Characterization by X-ray computed tomography of decohesion, porosity growth and coalescence in model metal matrix composites. Acta Mater 49(11):2055–2063
50. Roach AM, White BC, Garland A, Jared BH, Carroll JD, Boyce BL (2020) Size-dependent stochastic tensile properties in additively manufactured 316L stainless steel. Addit Manuf 32:101090
51. Hosseini E, Popovich VA (2019) A review of mechanical properties of additively manufactured Inconel 718. Addit Manuf 30:100877
52. Han Z, Luo H, Zhang Y, Cao J (2013) Effects of micro-structure on fatigue crack propagation and acoustic emission behaviors in a micro-alloyed steel. Mater Sci Eng, A 559:534–542
53. Wisner B (2019) Acoustic emission signal processing framework to identify fracture in aluminum alloys. Eng Fract Mech 210:367–380
54. Haneef T, Lahiri BB, Bagavathiappan S, Mukhopadhyay CK, Philip J, Rao BPC, Jayakumar T (2015) Study of the tensile behavior of AISI Type 316 stainless steel using acoustic emission and infrared thermography techniques. J Market Res 4(3):241–253
55. Chen G, Luo H, Yang H, Han Z, Lin Z, Zhang Z, Su Y (2019) Effects of the welding inclusion and notch on the fracture behaviors of low-alloy steel. J Market Res 8(1):447–456
56. Wisner B, Kontsos A (2018) In situ monitoring of particle fracture in aluminium alloys. Fatigue Fract Eng Mat Struct 41(3):581–596
57. Javanbakht M, Salahinejad E, Hadianfard MJ (2016) The effect of sintering temperature on the structure and mechanical properties of medical-grade powder metallurgy stainless steels. Powder Technol 289:37–43
58. Kumar N, Bharti A, Saxena KK (2020) A re-analysis of effect of various process parameters on the mechanical properties of Mg based MMCs fabricated by powder metallurgy technique. Mater Today: Proceedings 26:1953–1959